Hindawi Publishing Corporation
Mathematical Problems in Engineering
Volume 2015, Article ID 676457, 9 pages
http://dx.doi.org/10.1155/2015/676457

Research Article

Controlling Force in Polarization-Maintaining Fiber Fused Biconical Tapering

Wei Zhang,[1] Weibin Rong,[1] Lefeng Wang,[1] Qing Zheng,[2] and Lining Sun[1]

[1] *State Key Laboratory of Robotics and System, Harbin Institute of Technology, Harbin 150080, China*
[2] *AVIC Xi'an Flight Automatic Control Research Institute, Xi'an 710065, China*

Correspondence should be addressed to Weibin Rong; rwb@hit.edu.cn

Received 10 August 2014; Accepted 4 November 2014

Academic Editor: Junuthula N. Reddy

Fused biconical tapering (FBT) is an important method of manufacturing polarization-maintaining fiber (PMF) couplers. However, the tension on the ends of the fibers can affect the performance of the coupler. In this paper, a computer-based method of controlling the drawing force was presented. The system includes a drawing mechanism, rotary position encoders, and a control circuit. A three-dimensional model of a permanent magnet and a coil is constructed, and the relationship among the coil current, rotation angle of the clamp, and electromagnetic force is determined using finite element simulations. Electromagnetic force control based on these simulations can be realized. The method is verified experimentally, and it is shown that a drawing force of 0–1.8 gf can be achieved with an error of within 3.04%. This result can be used in the FBT-based manufacture of fiber components such as fiber couplers and gratings.

1. Introduction

Polarization-maintaining fiber (PMF) couplers are important passive components for achieving polarization light coupling, splitting, and multiplexing. They are widely used in fiber optic sensing and coherent communications [1, 2]. PMF couplers are typically fabricated using fiber biconical tapering (FBT) method, which involves fixing two optical fibers at a certain tension, heating the fibers to molten status, and drawing the fibers to form a biconical or dumbbell shape [3, 4]. Although the FBT method yields less extinction ratio of couplers than the polishing method, it has better thermal stability and smaller excess and insertion losses. FBT is controlled by three process parameters, the drawing speed, heating temperature, and drawing force, and the tension force on the fibers directly affects the performance of the PMF coupler. The translation stage in conventional FBT machines [5–8] consists of translation stage parts as well as heating and fiber clamping parts, and the translation stage parts are controlled with a computer to realize a precise drawing speed, but there is little control over the drawing force. Identically spring-loaded fiber pulling stages were introduced to impart a uniform tension to a pair of fibers, and this alleviated problems associated with sudden changes in the tension force [9]. However, the elongation of the spring changes the tension force on the fibers, which does not allow the tension force control during the drawing process. Our experiments have shown that crystallization of the fiber surface may occur when the drawing force is large, which will increase the excess loss. FBT is also an important method of manufacturing long-period fiber gratings, and the periodic decrease in the fiber cross section depends on the drawing force on the fiber. The drawing tension was usually controlled by clamping one end of the fiber to a translation stage and attaching a mass to the other end of the fiber to keep it under a constant axial tension [10, 11]. When the fiber is being drawn, however, the translation stage does not move at a constant velocity, so the tension in the optical fiber varies. It is difficult to adjust the tension in the fiber during the drawing process.

We propose here a computer-based method of controlling the drawing mechanism and drawing force during FBT. In the method, the drawing force is generated through the control of the coil current by detecting the rotation of the fiber clamp, which thus achieves semiclosed loop control. The drawing

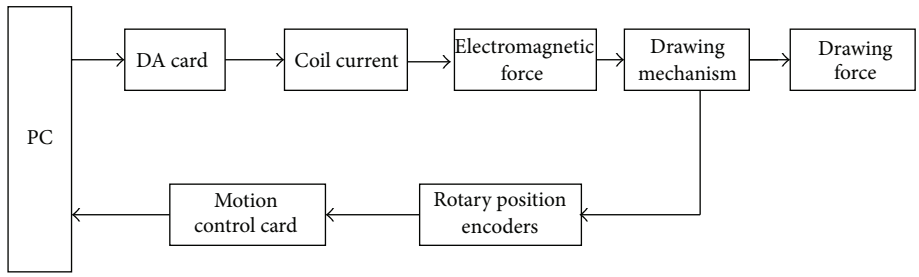

Figure 1: Block diagram of the force control system for the PMF FBT.

mechanism and control principle are introduced in Section 2. The force exerted on the permanent magnet by an electromagnetic coil is simulated using a three-dimensional (3D) finite element method in Section 3. Based on the analysis, a mathematical equation for the coil current, rotation angle of the fiber clamp, and electromagnetic force is established, and this equation is used to control the electromagnetic force. The drawing mechanism is analyzed and a simplified force model is presented in Section 4. In Section 5, we present the device used to detect the tension and an experimentally derived expression of the relationship among the coil current, rotation clamp angle, and drawing force. Control of the drawing force is also demonstrated in Section 5.

2. Setup and Control Method

The PMF fused taper drawing control system, shown in Figure 1, links the drawing mechanism, electromagnetic coil, rotary position encoders, digital-to-analog (DA) card, and motion control card to a personal computer (PC). The drawing mechanism (Figure 2) consists of a connect piece, drum wheel, fiber clamp, mass, permanent magnet, coil, and rotary position encoders.

The PC controls the current through the coil via the DA card to produce a certain magnetic field that interacts with the permanent magnet and generates the desired electromagnetic force. This causes the drawing force on the fiber clamp. As the two drum wheels are connected by two pieces, they rotate with the same rotation angle. The glass-disk rotary position encoders are linked to the drum wheel so that the rotary position encoders can detect the rotation angle. The drawing length of the clamped fibers is thus determined from the rotation angle. During the drawing, the distance between the permanent magnet and the coil changes so that the drawing force on the fiber clamp varies. The force can also be varied by changing the coil current in regard to the wheel rotation angle.

3. Analysis and Calculation of Electromagnetic Force

3.1. Theoretical Analysis. A cylindrical permanent magnet is used in the drawing mechanism. For a cylindrical permanent magnet that is magnetized along the z-direction with height

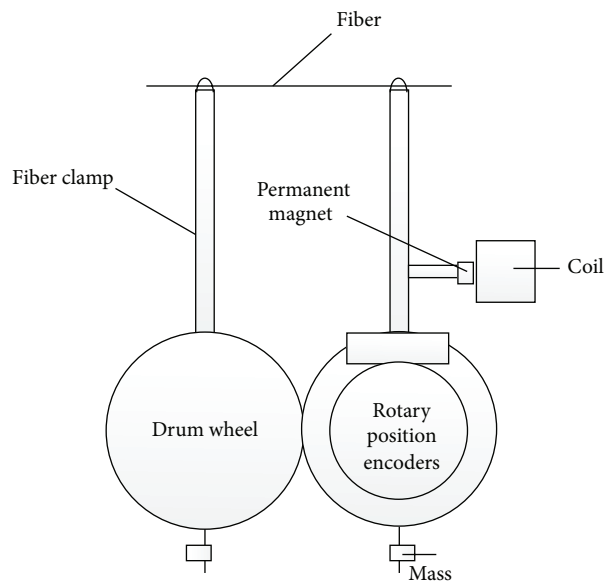

Figure 2: Structure of drawing mechanism.

Z_0 and radius a, the magnetic field distribution B at a point (r, ϕ, z) [12, 13] is

$$\begin{aligned} B_z &= \frac{\mu_0 J}{2\pi} \int_{-z_0/2}^{z_0/2} \frac{1}{\left[(a+r)^2 + (z-z')^2\right]^{1/2}} \\ &\quad \times \left[\frac{a^2 + r^2 - (z-z')^2}{(a-r)^2 + (z-z')^2} E(k) + K(k) \right] dz', \\ B_r &= \frac{\mu_0 J}{2\pi} \int_{-z_0/2}^{z_0/2} \frac{z-z'}{r\left[(a+r)^2 + (z-z')^2\right]^{1/2}} \\ &\quad \times \left[\frac{a^2 + r^2 + (z-z')^2}{(a-r)^2 + (z-z')^2} E(k) - K(k) \right] dz', \end{aligned} \tag{1}$$

where $K(k)$ and $E(k)$ are complete elliptic integrals of the first and second kind, respectively;

$$k = \sqrt{\frac{4ar}{(a+r)^2 + (z-z')^2}},$$

$$K[k] = \int_0^{\pi/2} \frac{1}{\sqrt{1 - k\sin^2(\phi)}} d\phi,$$
$$E[k] = \int_0^{\pi/2} \sqrt{1 - k\sin^2(\phi)} d\phi. \tag{2}$$

The electromagnetic force can be calculated using the Lorentz force method, Maxwell stress tensor method, or the virtual work method [14]. As the Lorentz force method is suitable for calculating the force of a carrier fluid in a magnetic field, it was chosen in this study. The electromagnetic force F_m applied to the permanent magnet and the electromagnetic force F_c applied to the current coil are action and reaction forces; that is,

$$F_m = -F_c = -\int_V f\, dv = -\int_V J \times B\, dv,$$
$$J = I \cdot \frac{N}{S}, \tag{3}$$

where f is the electromagnetic force per unit volume of the coil, J is the current density in the coil, B is the magnetic induction of the coil, I is the current in the coil of N turns, and S is the cross-sectional area of the coil wires.

3.2. Finite Element Analysis. The movement of the clamp is moving so that an accurate two-dimensional (2D) simulation cannot be performed when the cylindrical permanent magnet enters the coil. Thus, a 3D simulation model was created. The center of the drum wheel rotation defines the origin, with the x- and y-axes lying parallel to the length of the coil and fiber clamp, respectively. An insulating nylon frame was used for the coil, which is 24 mm long with inner and outer diameters of 20 and 40 mm, respectively, and consists of 1676 turns. $Nd_2Fe_{14}B$ was chosen as the material for the permanent magnet as it has a high energy product, coercive force, and energy density [15]. The surface magnetic induction of the permanent magnet was 389 mT, as measured by a Gauss meter (GV-300).

During the movement of the fiber clamp, the center of the permanent magnet and the angle vary with respect to the horizontal plane. Figure 3 shows a 2D view of the model structure in the $z = 0$ plane. Assuming that the center of the permanent magnet is at point B with coordinates of (p_x, p_y), then the coordinates of point B when the fiber clamp is rotated by an angle θ are

$$p_x = L_1 \sin\theta + L_2 \cos\theta,$$
$$p_y = L_1 \cos\theta + L_2 \sin\theta, \tag{4}$$

where L_1 and L_2 are the length of the A–O and A–B lines, respectively.

We created a cube of air with a side length of 130 mm to simulate the magnetic field distribution. This cube has insulating boundary conditions; that is, $\mathbf{n} \times \mathbf{A} = 0$, where $\mathbf{n}$ is the vector normal to the surface and $\mathbf{A}$ is the magnetic vector potential [16, 17]. Free tetrahedral elements are adopted in the finite element simulation. Finer meshes are used for the coil and permanent magnet to improve the accuracy and calculation speed, and fine meshes are used for the cube of air. A total of 44743 finite division elements were used. The electromagnetic force is obtained from the calculation of the Lorentz force.

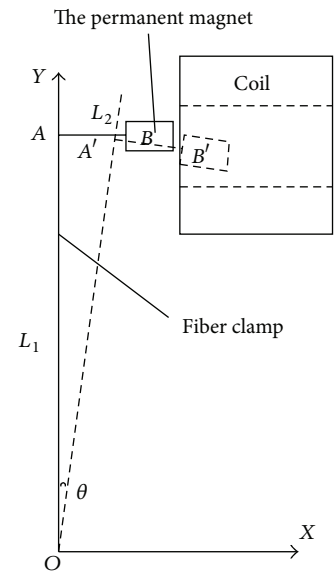

Figure 3: 2D schematic model of the drawing mechanism.

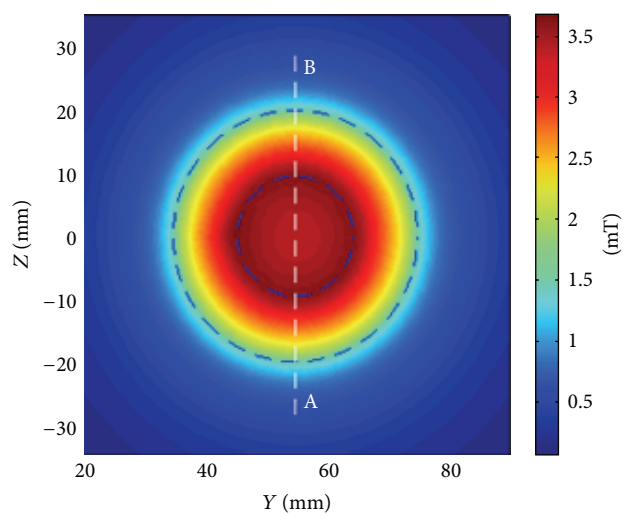

Figure 4: Simulated magnetic flux norm distribution at $x = 35$ mm.

3.3. Simulation Results. The magnetic flux norm distribution in the $x = 35$ mm plane, which is between the permanent magnet and the coil and 1 mm away from the coil, for a current of 0.1 A passing through the coil is shown in Figure 4. Figure 5 shows the distribution along the line A–B through the center of the coil. These results show that the magnetic flux norm is related to the distance from the coil center. Inside the inner coil radius, the magnetic flux norm decreases toward the center to a minimum of 3.41 mT. This value agrees

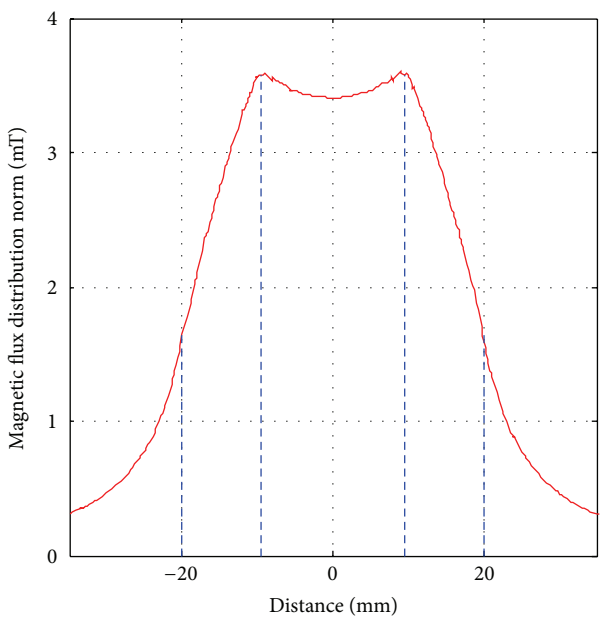

FIGURE 5: Magnetic flux norm along the line A–B in Figure 4.

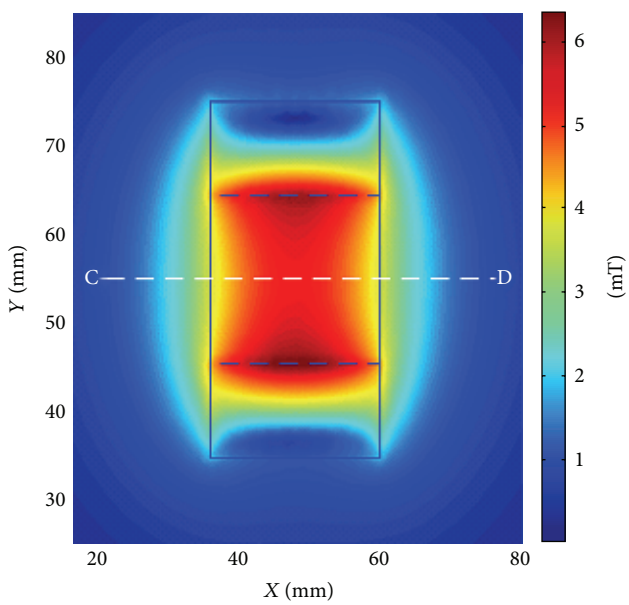

FIGURE 6: Simulated magnetic flux norm distribution at $z = 0$.

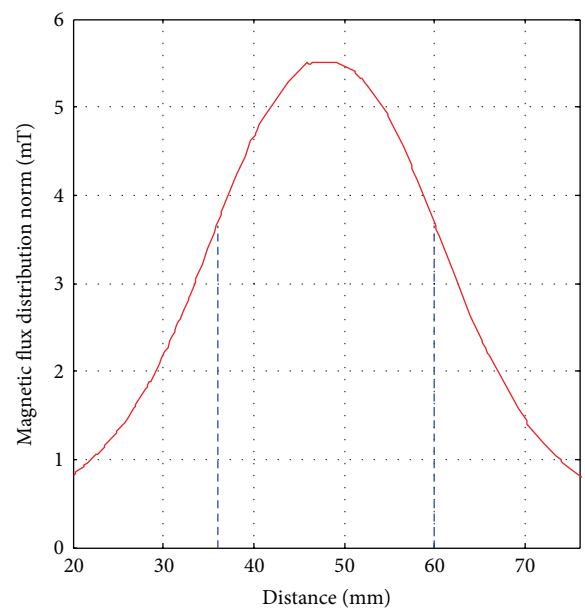

FIGURE 7: Simulated magnetic flux density norm along the line C–D in Figure 6.

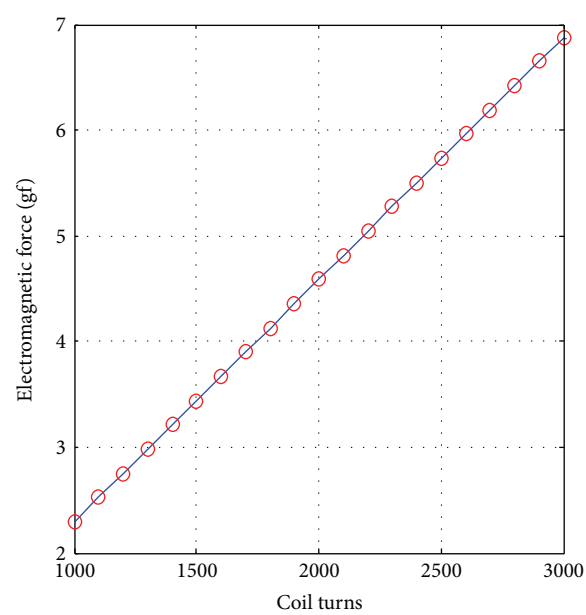

FIGURE 8: Simulated electromagnetic force as a function of the number of coil turns for $\theta = 0^\circ$ and $I = 0.1$ A.

well with the analytical value of 3.46 mT given in the literature [18]. The difference between the maximum and minimum magnetic flux norm value is 0.2 mT, which indicates that the rate of change is low. Outside the inner coil radius, the magnetic flux norm decreases rapidly with increasing distance from the maximum at the inner diameter of the coil. The magnetic flux distribution in the $z = 0$ plane which is shown in Figures 6 and 7 shows the distribution along the longitudinal axis of the coil (line C–D). The magnetic flux norm is symmetric about the longitudinal axis of the coil and achieves a maximum value at the center of the coil. Near the coil, the change in the magnetic flux norm is approximately linear.

Figure 8 shows the relationship between the electromagnetic force and the number of coil turns for $\theta = 0^\circ$ and $I = 0.1$ A. A least-squares fit of the data gives the linear relationship:

$$F_m = 0.0023N - 0.0026. \tag{5}$$

The number of coil turns, however, is fixed to $N = 1676$ for the simulations. Figure 9 shows the relationship between

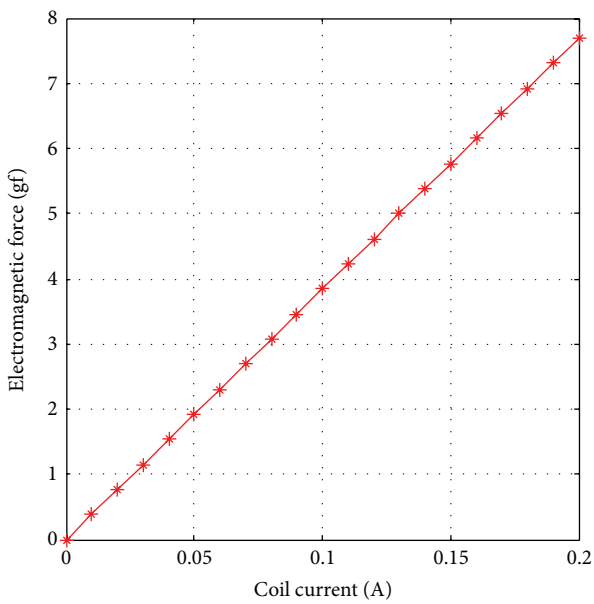

FIGURE 9: Simulated electromagnetic force as a function of the coil current for $\theta = 0^\circ$ and $N = 1676$.

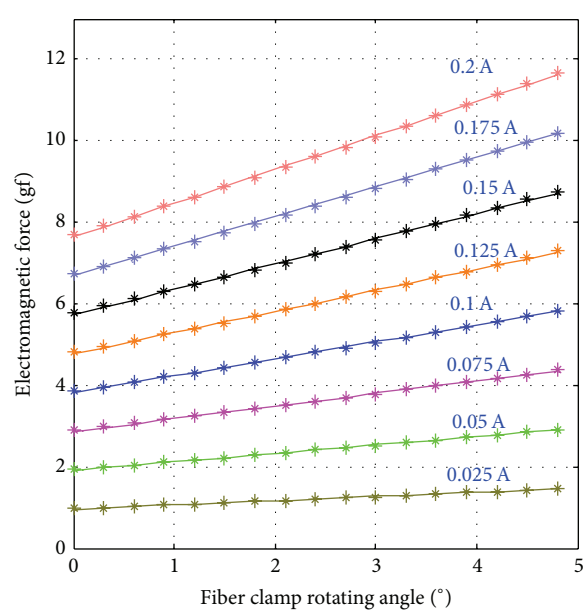

FIGURE 10: Simulated electromagnetic force as a function of the rotating angle for various coil currents.

the electromagnetic force and coil current for $\theta = 0^\circ$ and $N = 1676$, which also reveals linear behavior of

$$F_m = 38.4558I. \tag{6}$$

Changing the rotation angle θ of the clamp will change the position of the permanent magnet and hence the electromagnetic force. Figure 10 shows the relationship between the rotation angle θ and the electromagnetic force for a constant coil current. Again, we see a linear relationship, but the gradient, which is defined as the rate of change of

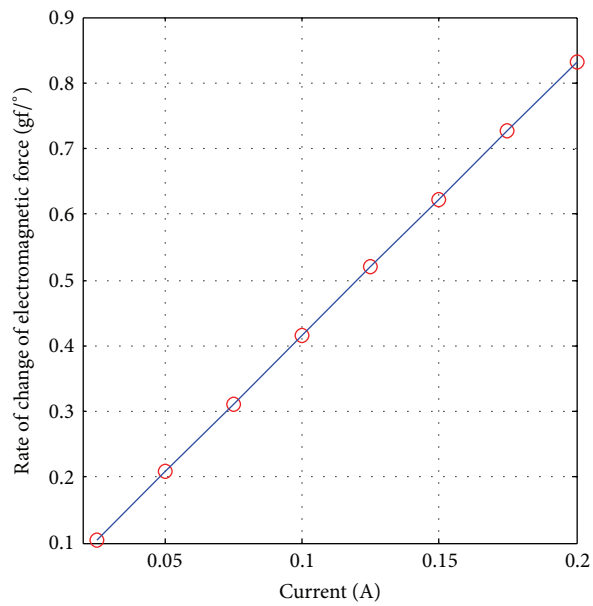

FIGURE 11: Simulated rate of change of the electromagnetic force as a function of the current.

the electromagnetic force, depends on the current. The gradient $K_{F\theta}$ can be expressed as

$$K_{F\theta} = \frac{\Delta F_m}{\Delta \theta}, \tag{7}$$

where ΔF_m is the change of the electromagnetic force of the permanent magnet (in units of gram-force) and $\Delta\theta$ is the change of the rotation angle of the clamp (in units of degrees). The rate of change of the electromagnetic force is shown as a function of the current in Figure 11. A linear fit gives

$$K_{F\theta} = 4.1517 \cdot I. \tag{8}$$

Changing θ will also change the relationship between the electromagnetic force and the current. For a constant angle, the electromagnetic force coefficient, K_{FI}, can be defined as

$$K_{FI} = \frac{\Delta F_m}{\Delta I}, \tag{9}$$

where ΔI is the change of the coil current (in units of amperes). Figure 12 shows K_{FI} as a function of the rotating angle (0° to 4.8°), and a linear fit yields

$$K_{FI} = 4.1517\theta + 38.1982. \tag{10}$$

We thus obtain a mathematical expression for the relationship among F_m, I, and θ:

$$I = 0.026F_m - \frac{0.108F_m\theta}{(4.1517\theta + 38.1982)}. \tag{11}$$

The electromagnetic force can be controlled by adjusting the coil current on the basis of (11). Figure 13 shows that a relatively constant electromagnetic force can be achieved for fiber clamp rotating angles from 0° to 4.8° once the coil current control is implemented. Table 1 lists the simulation error of the electromagnetic force, and it indicates that the force can be controlled accurately with an error of about 1%.

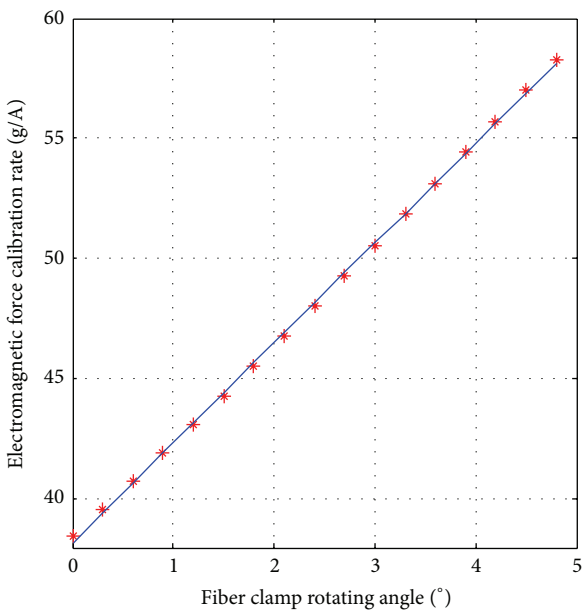

Figure 12: Simulated electromagnetic force calibration rate as a function of the rotating angle.

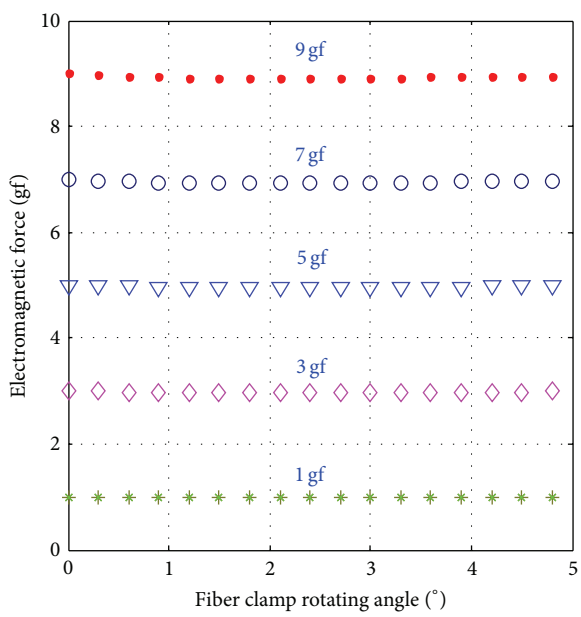

Figure 13: Simulated electromagnetic force as a function of the rotating angles after implementing current control.

Table 1: Simulated control error.

Electromagnetic force (gf)	1	3	5	7	9
Error (%)	0.98	1.03	1.03	1.02	1.01

4. Drawing Force Analysis

The drawing mechanism contains two spring pieces that are used to connect the two drum wheels and maintain equal clamp rotation angles. The bending elastic force of the two pieces can be neglected as it is considerably smaller than the drawing force. As the drawing force and the rotation angles of the clamps are equal, the following analysis can be performed for a single clamp (in this case, the clamp on the right). Figures 14 and 15 outline the force and torque components for the analysis of the two clamps. For a rotation angle of 0°–5°, the torque-balanced expression for the fiber holders is

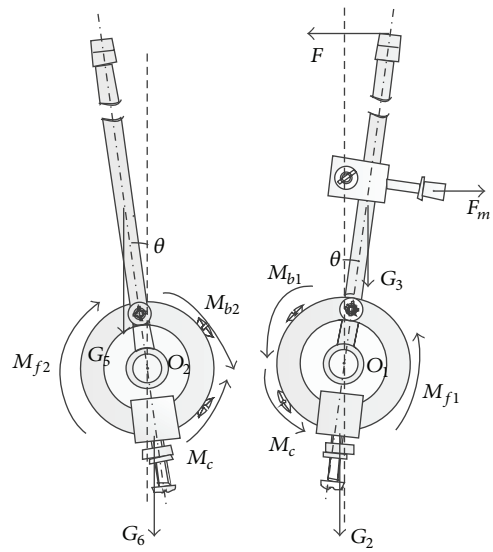

Figure 14: Force and moment analysis model of two separate clamps.

$$M_{G6} + M_{b2} + M_{f2} = M_{G5} + M_c, \tag{12}$$

$$\begin{aligned} M_{G2} + M_{b1} + M_{f1} + F \cdot L_F \cdot \cos\theta + M_c \\ = M_{G3} + F_m \cdot L_m \cdot \cos\theta, \end{aligned} \tag{13}$$

where M_{b2} (M_{b1}) is the torque generated by the spring piece and fastening bolts on the left (right) fiber clamp; M_{f2} (M_{f1}) is the torque generated by friction during the rotation of the left (right) fiber clamp; M_{G6} (M_{G2}) is the torque generated by the mass on the bottom of the left (right) fiber clamp; M_{G5} is the torque generated by the left fiber clamp; M_{G3} is the torque generated by the right fiber holder, permanent magnet, and fixed base; F is the drawing force generated by the right fiber clamp; L_F is the distance between the rotation center O_1 and the application point of F_1 for $\theta = 0°$; L_m is the distance between the application point of F_m and O_1 for $\theta = 0°$; and M_c is the torque generated by the connect piece. From (12), we see that M_{G6} can be varied by adjusting the position of the mass on the left fiber holder such that M_c will be zero. The position of the mass on the bottom of the right fiber clamp is then adjusted so that M_{G2} satisfies

$$M_{G2} + M_{b1} + M_{f1} = M_{G3}. \tag{14}$$

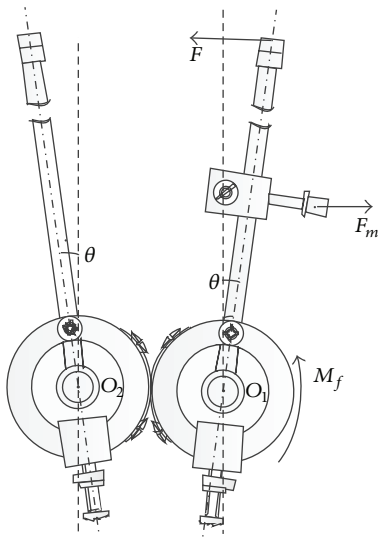

Figure 15: Overall force and moment analysis model of the clamps.

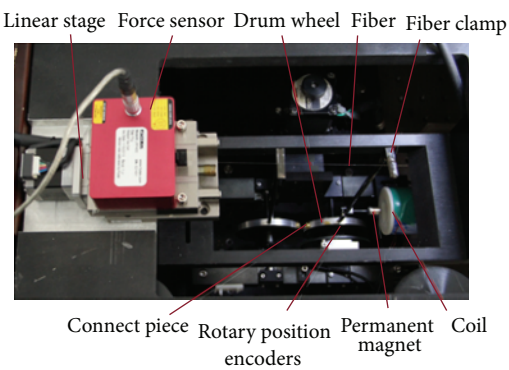

Figure 16: Drawing force detection device.

The mechanical force of the drawing mechanism is thus described in Figure 15, and the drawing mechanism then satisfies the torque balance equation

$$M_{f1} + F \cdot L_F \cdot \cos\theta = F_m \cdot L_m \cdot \cos\theta. \tag{15}$$

The drawing mechanism used in this study has precision deep groove ball bearings that have a friction coefficient of 0.001–0.0015. The friction during the fiber clamp rotation is also small by comparison with the drawing force and can also be neglected. Thus, (15) can be simplified as

$$F = F_m \cdot \frac{L_m}{L_F}. \tag{16}$$

When the right clamp is at 0° and the coil current is 0.1 A, the theoretical value of the electromagnetic force is 3.8437 gf, which yields a drawing force of 1.127 gf according to (16).

5. Force Detection Experiment

The experimental force detection device, shown in Figure 16, includes a precision electric linear stage, force sensor, and the control system shown in Figure 1. The linear stage has a repeat accuracy of 1 μm. The force sensor has a resolution of 0.1 mgf and is fixed on the linear stage connected to the right fiber clamp by the fiber. The rotation of the fiber clamp is controlled by the motion control card in the PC through the linear stage. Setting the rotation angle of the right fiber clamp to zero and the coil current to 0.100 A yields a drawing force on the right fiber clamp end of 0.9952 gf, which is in reasonable agreement with the simulation result of 1.127 gf.

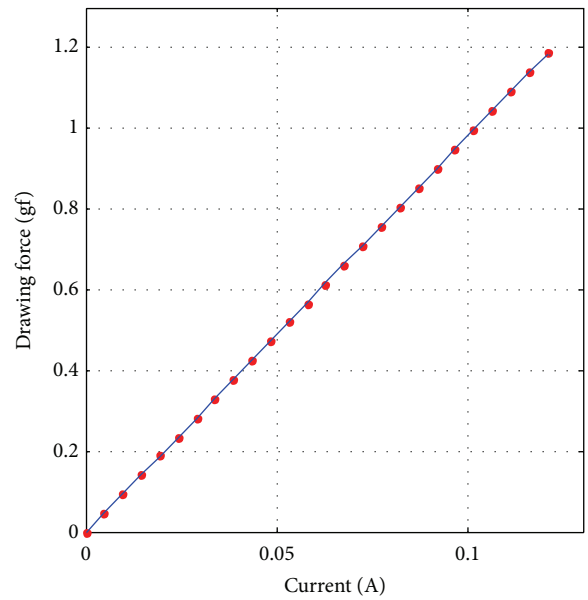

Figure 17: Experimental drawing force as a function of the coil current.

For a rotating angle of zero, the relationship between the drawing force and current is linear, as was shown in Section 3, and to confirm this experimentally the drawing force F was measured for currents of 0 to 0.2 A (Figure 17). A fit to the experimental data gave

$$F = 9.8512I - 0.0027, \tag{17}$$

which includes a nonzero constant owing to friction and assembly errors.

The drawing force is shown as a function of the rotating angle (0° to 4.8°) in Figure 18 for various coil currents. As predicted by the simulations, there is a linear relationship between the drawing force and the rotating angle, and the rate of change of the drawing force (Figure 19) is given by

$$K_{F\theta} = 0.7119I_c - 0.0078. \tag{18}$$

Figure 20 shows the drawing force calibration rate as a function of the rotating angle, which can be expressed as

$$K_{FI} = 0.7133\theta + 9.9860. \tag{19}$$

The relationship among F, I, and θ can then be summarized as

$$I_c = 101.5F + 0.2741 - \frac{1000\,(723F - 76)\,\theta}{(7133\theta + 99860)}. \tag{20}$$

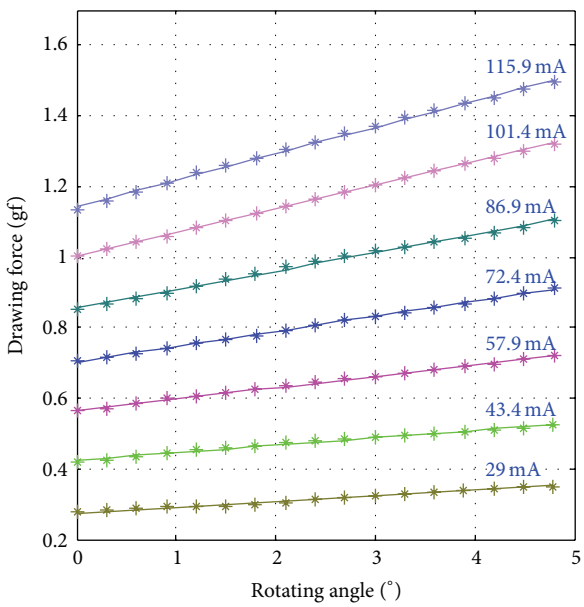

FIGURE 18: Experimental drawing force as a function of the rotating angle for various coil currents.

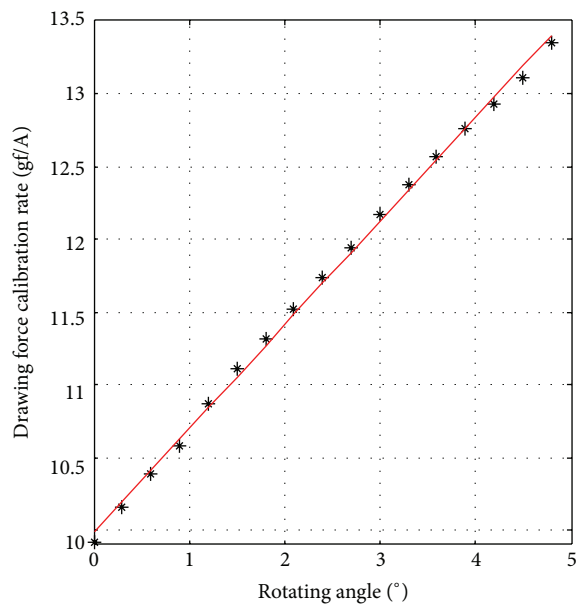

FIGURE 20: Experimental drawing force calibration rate as a function of the rotating angle.

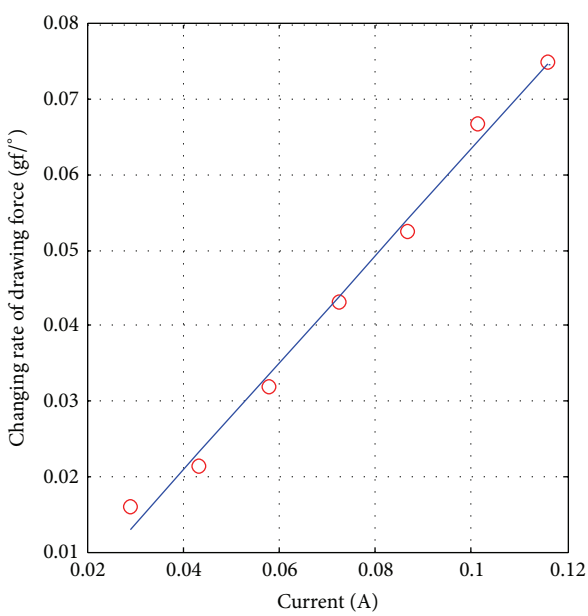

FIGURE 19: Experimental rate of change of the drawing force as a function of the current.

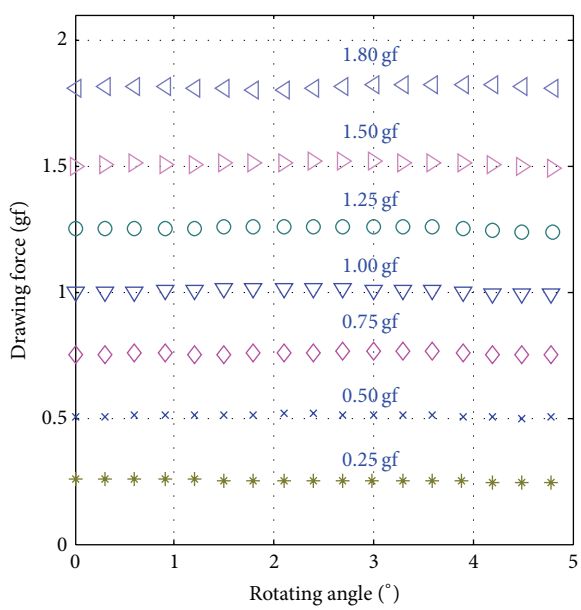

FIGURE 21: Experimental drawing force as a function of the rotating angle after implementing current control.

The rotation angle of the clamp, detected by the rotary position encoders, can thus be used in determining the current to apply to the coil, which is controlled by the DA output voltage, for a known drawing force. In this way, the drawing force can be controlled. Figure 21 shows the drawing force as a function of the rotating angle after implementing the current control, and the errors in the experimental control are listed in Table 2. The maximum error generated by a constant force is 3.04%. A maximum force of 1.8 gf was obtained, but (5) and (17) indicate that a higher force can be applied by increasing the number of turns and the coil current.

TABLE 2: Experimental control error.

Drawing force (gf)	0.25	0.5	0.75	1	1.25	1.5	1.8
Error (%)	2.48	3.04	2.23	1.28	1.00	1.18	1.36

6. Conclusion

The drawing force applied to the fibers can affect the coupling performance in PMF FBT, and we have proposed a method for controlling the force during FBT. We constructed a 3D model of the permanent magnet in the drawing mechanism and established an equation of motion for the magnet. We developed an expression for the relationship among the coil current, rotation angle of the fiber clamp, and the electromagnetic force by simulation and used this expression to control the electromagnetic force; the calculation error was within 1.03%. The mechanical model of the stretching mechanism was simplified by adjusting the mass, and the relationship between the drawing force on the fiber clamp and the electromagnetic force was established. The relationship among the coil current, rotation angle of the clamp, and drawing force was confirmed experimentally, and experimental control of the driving force (0–1.8 gf) was accurate enough with an error less than 3.04%. The results presented here have verified the feasibility of the proposed control method for FBT. Using this method, the drawing force on the fibers can be controlled effectively.

Conflict of Interests

The authors declare that there is no conflict of interests regarding the publication of this paper.

Acknowledgments

This research was supported by Self-Planned Task of State Key Laboratory of Robotics and System (SKLRS201301A01) and the Program for Changjiang Scholars and Innovative Research Team in University (IRT0915).

References

[1] D. P. Davé, T. Akkin, and T. E. Milner, "Polarization-maintaining fiber-based optical low-coherence reflectometer for characterization and ranging of birefringence," *Optics Letters*, vol. 28, no. 19, pp. 1775–1777, 2003.

[2] M. Bin and X. Jian, "Experimental research of coupling fiber-optic sensor for vibration measurement," in *Proceedings of the International Symposium on Photonics and Optoelectronics (SOPO '10)*, pp. 1–4, IEEE, Chengdu, China, June 2010.

[3] B. S. Kawasaki, K. O. Hill, and R. G. Lamont, "Biconical-taper single-mode fiber coupler," *Optics Letters*, vol. 6, no. 7, pp. 327–328, 1981.

[4] R. G. Lamont, D. C. Johnson, and K. O. Hill, "Power transfer in fused biconical-taper single-mode fiber couplers: dependence on external refractive index," *Applied Optics*, vol. 24, no. 3, pp. 327–332, 1985.

[5] S. W. Harun, K. S. Lim, C. K. Tio, K. Dimyati, and H. Ahmad, "Theoretical analysis and fabrication of tapered fiber," *Optik*, vol. 124, no. 6, pp. 538–543, 2013.

[6] C. S. Hsieh, T. L. Wu, and W. H. Cheng, "Optimum approach for fabrication of low loss fused fiber couplers," *Materials Chemistry and Physics*, vol. 69, no. 1–3, pp. 199–203, 2001.

[7] Y. Wang and H. Liu, "The comparison of two methods to manufacture fused biconical tapered optical fiber coupler," in *Photonics and Optoelectronics Meetings (POEM) 2009: Fiber Optic Communication and Sensors*, vol. 7514 of *Proceedings of SPIE*, October 2009.

[8] C. Shuai, C. Gao, Y. Nie, H. Hu, and S. Peng, "Microstructure analysis in the coupling region of fiber coupler with a novel electrical micro-heater," *Optical Fiber Technology*, vol. 17, no. 6, pp. 541–545, 2011.

[9] B. P. Pal, P. R. Chaudhuri, and M. R. Shenoy, "Fabrication and modeling of fused biconical tapered fiber couplers," *Fiber and Integrated Optics*, vol. 22, no. 2, pp. 97–117, 2003.

[10] F. Dürr, G. Rego, P. V. S. Marques et al., "Tomographic stress profiling of arc-induced long-period fiber gratings," *Journal of Lightwave Technology*, vol. 23, no. 11, pp. 3947–3953, 2005.

[11] G. Rego, O. Okhotnikov, E. Dianov, and V. Sulimov, "High-temperature stability of long-period fiber gratings produced using an electric arc," *Journal of Lightwave Technology*, vol. 19, no. 10, pp. 1574–1579, 2001.

[12] B. Ebrahimi, M. B. Khamesee, and M. F. Golnaraghi, "Design and modeling of a magnetic shock absorber based on eddy current damping effect," *Journal of Sound and Vibration*, vol. 315, no. 4-5, pp. 875–889, 2008.

[13] J. S. Agashe and D. P. Arnold, "A study of scaling and geometry effects on the forces between cuboidal and cylindrical magnets using analytical force solutions," *Journal of Physics D: Applied Physics*, vol. 41, no. 10, Article ID 105001, 2008.

[14] Y.-D. Chun and J. Lee, "Comparison of magnetic levitation force between a permanent magnet and a high temperature superconductor using different force calculation methods," *Physica C: Superconductivity*, vol. 372–376, part 3, pp. 1491–1494, 2002.

[15] N. Leventis and X. Gao, "Nd-Fe-B permanent magnet electrodes. Theoretical evaluation and experimental demonstration of the paramagnetic body forces," *Journal of the American Chemical Society*, vol. 124, no. 6, pp. 1079–1088, 2002.

[16] A. Alferenok, M. Werner, M. Gramss, U. Luedtke, and B. Halbedel, "Numerical optimization of the magnet system for the Lorentz Force Velocimetry of electrolytes," *International Journal of Applied Electromagnetics and Mechanics*, vol. 38, no. 2-3, pp. 79–92, 2012.

[17] M. Ziolkowski and H. Brauer, "Fast computation technique of forces acting on moving permanent magnet," *IEEE Transactions on Magnetics*, vol. 46, no. 8, pp. 2927–2930, 2010.

[18] C. Pawashe, S. Floyd, and M. Sitti, "Modeling and experimental characterization of an untethered magnetic micro-robot," *International Journal of Robotics Research*, vol. 28, no. 8, pp. 1077–1094, 2009.